Applied Surface Science 695 (2025) 162847

Contents lists available at ScienceDirect

Applied Surface Science

journal homepage: www.elsevier.com/locate/apsusc

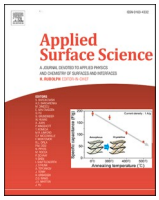

Full Length Article

Enhanced corrosion resistance of magnesium alloy via surface transfer of microwave-synthesized, non-toxic, and ultra-smooth nitrogen-doped amorphous carbon thin film

Adarsh Rai [a,b,*], Mateusz Szczerba [b,c], Joanna Karbowniczek [a], Kamil Cichocki [a], Michal Krzyzanowski [a,d], Szymon Bajda [a], Grzegorz D. Sulka [b], Michał Szuwarzyński [e], Krystian Sokołowski [e], Björn Wiese [f]

[a] Faculty of Metals Engineering and Industrial Computer Science, AGH University of Krakow, Mickiewicza 30, Krakow 30-059, Poland
[b] Department of Physical Chemistry and Electrochemistry, Faculty of Chemistry, Jagiellonian University, Gronostajowa 2, 30-387, Krakow, Poland
[c] Doctoral School of Exact and Natural Sciences, Jagiellonian University, Lojasiewicza 11, 30-348 Krakow, Poland
[d] Birmingham City University, Millennium Point, Curzon Street, Birmingham B4 7XG, UK
[e] Academic Centre for Materials and Nanotechnology, AGH University of Krakow 30-059 Krakow, Poland
[f] Helmholtz-Zentrum Hereon, Institute of Metallic Biomaterials, Functional Magnesium Materials, Max-Planck-Straße 1, Geesthacht 21502, Germany

ARTICLE INFO

Keywords:
Amorphous carbon thin film
Film transfer
Magnesium alloy
Corrosion resistance
Cytotoxicity

ABSTRACT

Magnesium (Mg) alloys are increasingly recognized as a promising material for the next generation of implants due to their biocompatibility, favorable mechanical strength, and ability to biodegrade effectively in physiological environments. However, their clinical utility is hindered by rapid corrosion. This study introduces and investigates the application of an ultrathin, ultrasmooth, and corrosion-resistant nitrogen-doped amorphous carbon (a-C:N) thin film on a magnesium alloy (Mg-0.5Zn-0.2Ca) for the first time. The a-C:N film was synthesized using a polymer composite based on branched polyethyleneimine and subsequently applied to the magnesium alloy surface to enhance its corrosion resistance. Comprehensive characterization using advanced techniques confirmed the amorphous nature of the synthesized film, revealing the presence of sp^2-C, sp^3-C, and C-N bonds. AFM analyses and electrochemical corrosion tests demonstrated that the synthesized a-C:N film exhibits excellent corrosion resistance and reduces the corrosion rate of the substrate. Additionally, cytotoxicity tests indicated that the film is non-toxic and compatible for orthopedic implant applications, thereby expanding the potential clinical use of Mg-based implants. Carbon, being a biocompatible and inert nonmetallic element, makes it a suitable choice for enhancing the biocompatibility and corrosion resistance of Mg-based implants.

1. Introduction

For many years, orthopedic problems such as osteoporosis, osteoarthritis, bone fractures (including open fractures), nonunion fractures, and bone tumor removal have posed significant challenges for healthcare systems [1,2]. These problems require long-term treatment and are often associated with high complication rates and costs, and place substantial burdens on patients and their families. Despite the widespread use of both autografts- tissue from the patient's own body- and allografts- tissue from a donor- in clinical treatments, both methods have several limitations. For instance, autografts may be inadequate for treating large-area defects, while allografts carry a risk of immunological rejection [3]. In the search of innovative biomaterials for improved implant devices, biodegradable implantable materials like polymers and ceramics offer the advantage of gradual degradation and full resorption by the body [4]. However, their poor mechanical properties, brittleness, and potential to cause adverse tissue responses present significant barriers for clinical application. Research indicates that the degradation byproducts of these polymers may provoke unfavorable tissue reactions, making them unsuitable for use in clinical implants [5,6].

In recent years, magnesium and its alloys have demonstrated significant promise as implant materials compared to polymeric or other metallic alternatives. Their mechanical properties closely resemble

* Corresponding author.
E-mail address: rai@agh.edu.pl (A. Rai).

https://doi.org/10.1016/j.apsusc.2025.162847
Received 30 December 2024; Received in revised form 23 February 2025; Accepted 28 February 2025
Available online 1 March 2025

those of natural bone, which helps mitigate stress shielding effects, thereby reducing the risk of inflammation and refractures during implantation. Magnesium alloys offer an appealing combination of low density, high strength-to-weight ratio, and exceptional dimensional stability [7,8]. With a Young's modulus ranging from 41 to 45 GPa, these materials are much closer to that of human bone (10 to 40 GPa) than alternatives such as titanium alloys, 316L stainless steel, and cobalt-based alloys, which have Young's moduli of 110 GPa, 189 GPa, and over 230 GPa, respectively [9]. Moreover, magnesium's biodegradability eliminates the need for secondary implant removal procedures and facilitates new bone growth through the release of magnesium ions [10]. However, a key challenge with magnesium-based implants is their rapid degradation in the body, which occurs much faster than with inert metals like titanium alloys and stainless steels [9,11]. This rapid degradation leads to generation of hydrogen gas and significant changes in local alkalinity, which can compromise the mechanical integrity of the implant before the healing process is completed [12–14]. To ensure the long-term stability of magnesium-based implants during healing, it is critical to improve the surface corrosion resistance of magnesium and its alloys.

Several strategies have been employed to address the issue of magnesium's rapid degradation, including alloying, surface modification, and coatings, all aimed at enhancing the corrosion resistance of pure magnesium and its alloys [15–20]. In surface modifications, the physical vapor deposition (PVD), chemical conversion, sol–gel, micro-arc oxidation, and electrodeposition are some of the techniques that have been investigated [21]. Among PVD, Arc ion planting is significantly utilized in industries because of its high rates of ionization and deposition. However, due to the emissions of macroparticles, it often results in notable surface roughness and low coating density [22,23]. To provide smoother, denser coatings, the magnetically filtered cathode vacuum arc (FCVA) approach was developed. This method successfully eliminates large particles [24,25]. However, FCVA may be constrained by its increased operational expenses and complexity. Whereas, the use of microwave-synthesized, polymer-based thin films over the surface of metals has shown promising results in enhancing the degradability of metals, while maintaining low complexity and cost [26].

Amorphous carbon, with its mix of sp^2 and sp^3 bonds, offers high chemical stability, wear resistance, and biocompatibility, making it ideal for implants. The coating performance depends on the sp^3/sp^2 balance: sp^3 enhances mechanical strength, while sp^2 improves electrical conductivity. However, high internal stress can lead to coating failure [27]. Recent advances in deposition techniques show that doping with nitrogen has several advantages. Nitrogen improves hydrophilicity and cellular adhesion, while tuning the sp^2/sp^3 ratio further optimizes biocompatibility [28]. Several other methods of preparation of nitrogen doped amorphous carbon coating have been developed to modify metals. For instance, the use of nitrogen doped diamond-like carbon (DLC) coatings [23], hydrogen-free DLC coatings [25], utilization of chemical vapor deposition [29] to apply a nitrogen-doped amorphous film onto a copper substrate, demonstrating beneficial properties such as hydrophobicity, nano-scale thickness, and resistance to ion transport. Superhydrophobic coatings and graphene-based coatings have shown potential in enhancing corrosion resistance. Despite their effectiveness, these coatings often involve complex preparation processes, while graphene-based composite coatings tend to be costly [29–32]. As a result, there is a growing need for an eco-friendly, low-cost, easily accessible, and effective nitrogen-doped amorphous carbon coating for corrosion protection of magnesium alloy.

To address these limitations, in this study we use branched polyethyleneimine (b- PEI) with glucose in specific proportions to synthesize a biocompatible nitrogen doped amorphous carbon (a-C:N) thin film. The synthesis of the a-C:N film was carried out using microwave technology, followed by its transfer onto the surface of a targeted magnesium alloy. In this work, the synthesized a-C:N film was easily and directly transferred onto the magnesium alloy for the first time, remaining undamaged and attached throughout the study. This approach not only demonstrates a novel method for coating magnesium alloys but also addresses existing gaps in the literature regarding the direct transfer of a-C:N films onto magnesium-based substrates, their stability, and their corrosion resistance in biologically relevant environments. Additionally, this is a rapid, direct single step, low-cost synthesis method on target substrate with significant scalability as compared to other synthesis processes like chemical or physical vapor deposition, pulsed laser deposition, sputtering, filtered cathodic carbon arc evaporation. After the film transfer, its corrosion resistance was assessed through electrochemical corrosion tests, and immersion tests were conducted to observe morphological changes. Additionally, the cytotoxicity tests of the coated samples were evaluated using cell assays to determine the cytotoxicity of the film in relation to the underlying alloy.

2. Materials and methods

2.1. Mg alloy: Preparation

The magnesium alloy (Mg-0.5Zn-0.2Ca) was fabricated using the direct-chill casting process. The raw materials included pure Mg (99.95 wt% Magnesium Elektron Ltd., UK), Zn (99.99 wt% Wilhelm Grillo Handelsgesellschaft GmbH, Germany), and Ca (99.51 wt% Alfa Aesar GmbH & Co KG, Germany). The alloy melt was maintained at the temperature of 720 °C in an Ar-SF6 protective environment before being cast into molds. The steel molds were pre-heated to 680 °C and coated with boron nitride. The melt was solidified in the prepared molds via water quenching, producing cylindrical casting ingots with a length of 180 mm and a diameter of 65 mm. To achieve a more homogeneous microstructure, the ingots were subjected to solution annealing at 450 °C for 16 h, followed by quenching in cold water at room temperature. The chemical composition test of the Mg-0.5Zn-0.2Ca alloy was carried out using a SPECTRAMAXx emission spectrometer with spark excitation.

2.2. a-C:N film: Synthesis and transfer

Fig. 1 schematically illustrates the synthesis of nitrogen doped ultrathin amorphous carbon (a-C:N) film and its subsequent transfer onto the entire targeted metal surface. The precursor solution for the a-C:N film was prepared by mixing branched polyethyleneimine (b-PEI, MW 25 000, Sigma Aldrich, Merck Life Science Pvt. LTD) and D-(+) glucose (Merck Life Science Pvt. LTD). Initially, a 60 mg/ml solution of b-PEI was prepared in distilled water using ultrasonication. Additionally, a 1.5 M aqueous solution of D-(+) glucose was prepared by dissolving D-(+) glucose in distilled water with a vortex shaker. The two solutions were then mixed in a 1:1 vol ratio, followed by vortex mixing, and left to stand for 12 h.

Just before spin coating, the solutions were filtered through a 0.45 mm polyvinylidene fluoride (PVDF) filter. A p-doped conductive Si wafer (10 S/cm) with a 300 nm SiO_2 layer was treated with O_2-plasma for 5 min at 200 W. The filtered precursor solution was spin-coated onto the wafer at 2000 rpm for 20 s. The film was softly baked on a hot plate at 70 °C, then placed in a microwave oven, where it was irradiated with 260 W of microwave power for 90 s. The wafer was allowed to cool in air at room temperature and was subsequently washed with water, ethanol, and acetone. The thickness of the a-C:N thin film can be adjusted by varying the concentration of b-PEI and glucose in the precursor solution as well as the spin coating conditions.

For the transfer of the ultrathin a-C:N film onto a metal alloy, a 6 wt% solution of poly(methyl methacrylate) (PMMA, Sigma Aldrich, average MW ≈ 350,000 by GPC) was spin-coated on top of the as-synthesized a-C:N thin film. The PMMA-coated sample was soft baked on a hot plate at 70 °C for 5 min and then at 90 °C for 10 min. The sample was then immersed in a diluted HF solution (0.3 wt%) to etch the thick SiO_2 layer,

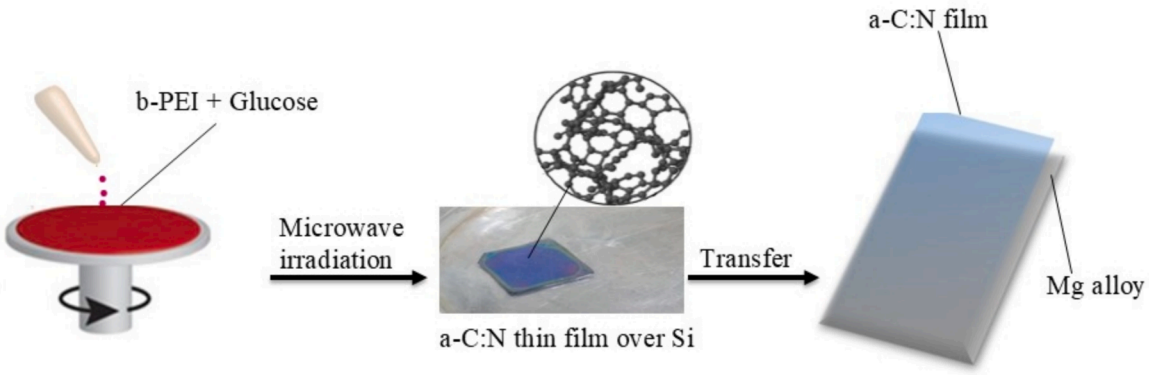

Fig. 1. Schematic representation of the microwave-assisted synthesis of the nitrogen-doped ultra-thin amorphous carbon film. The process involves the preparation of an aqueous solution of b-PEI and aqueous solution of glucose. The as-synthesized film was transferred onto the entire surface of the targeted metal substrate.

allowing the PMMA-coated a-C:N film to float on the pure water surface. The film was carefully transferred onto metal alloy samples which were circular with a radius of 3.5 mm and a thickness of 0.5 mm. Finally, the PMMA layer was removed by dissolving it in dichloromethane.

2.3. Characterization

The topology, thickness, and conducive parameters of the film were examined using atomic force microscopy (AFM) using a Dimension Icon XR microscope (Bruker, Santa Barbara, CA, USA) operating in the air under PeakForce Tapping (PFT) mode. Standard silicon cantilevers were used with a nominal spring constant of 0.4 N/m, triangular tip geometry, and a nominal tip radius of 2 nm.

The elemental composition and bonding configuration of the synthesized film were determined through X-ray photoelectron spectroscopy (XPS) using a PHI VersaProbe II Scanning XPS system, which employed monochromatic Al Kα (1486.6 eV) X-rays focused on a 100 μm spot. The photoelectron take-off angle was set at 45°, with the analyzer pass energy set to 117.50 eV for survey scans and 46.95 eV for high resolution spectra. Dual beam charge compensation, using 7 eV Ar^+ ions and 1 eV electrons, was applied to maintain a stable surface potential regardless of sample conductivity. All XPS spectra were referenced to the unfunctionalized, saturated carbon (C—C) C 1 s peak at 285.0 eV. The operating pressure in the analytical chamber was maintained at less than 3×10^{-9} mbar. Deconvolution of spectra was carried out using PHI MultiPak software (v.9.9.3) with background subtraction performed using the Shirley method. Functional group analysis of the film was conducted using Fourier transform infrared (FTIR) spectroscopy with a PerkinElmer spectrophotometer, with spectra recorded in the range of 400–4000 cm^{-1}. To further characterize the amorphous nature of the film, X-ray diffraction study (XRD) was performed using a powder X-ray diffractometer (Bruker D8 Advance eco) having a copper X-ray tube with CuKα radiation (λ = 1.5418 Á, 25A, 40 V). The Scanning rate was 2° per minute in the 2 Θ range from 10°−70°. High Resolution Transmission Electron Microscope (HR- TEM) employed using Tecnai G2 20 TWIN, FEI Company of USA (S.E.A.) PTE, LTD.

The morphological and structural evaluation of the film was carried out via scanning electron microscopy (SEM) and energy-dispersive X-ray spectroscopy (EDS) using an Inspect S50 microscope (FEI, USA) with an Octane Elect EDS detector. SEM images were captured both before and after immersion in dilute HCl (pH 6.9) and phosphate-buffered saline (PBS, pH 7.4) at room temperature. Additionally, Raman Spectrum was obtained by LabRAM HR Evolution by Horiba Inc. with the wavelength of laser excitation 633 nm and spot size of laser excitation was 721 nm.

2.4. Electrochemical corrosion tests

Potentiodynamic polarization curves were obtained using an electrochemical workstation (Biologic, SP-300 potentiostat, operated via EC-Lab® software). Electrochemical corrosion tests were conducted in 50 ml of Phosphate-Buffered Saline (PBS) solution of pH 7.4 and 37 °C, utilizing a three-electrode cell setup. A magnesium alloy was used as the working electrode, a platinum mesh served as the counter-electrode, and an Ag/AgCl, saturated KCl electrode was employed as the reference electrode. All samples were sealed with a silicon rubber sheath, exposing a working surface area of 0.785 cm^2. Before measurements, the electrodes were immersed into the PBS solution at Open Circuit Potential (OCP) for 1 h at 37 °C to allow for stabilization. The testing equipment was placed inside a Faraday cage to minimize electromagnetic interference. The EIS tests were registered with a 10^{-2}H z to 10^5 Hz range and an amplitude of 10 mV at Open Circuit Potential (OCP). The data were then fitted by ZSimpWin software using the opportune equivalent circuit. The potentiodynamic polarization tests were carried out using a scan rate of 1 mV/s, ranging from − 0.3 V to 0.3 V. The natural corrosion current (I_{corr}), natural corrosion potential (E_{corr}), cathodic Tafel slope (β_c), and the anodic Tafel slope (β_a) were determined by using Tafel extrapolation.

2.5. Cytotoxicity test with MG-63 cell line (osteoblast-like cells)

Samples were incubated in cell culture medium containing Dulbecco's Modified Eagle Medium supplemented with 10 % fetal bovine serum (FBS), 2 % antibiotics (penicillin/streptomycin), 1 % amino acids, and 1 % L-glutamine (all reagents from Sigma-Aldrich, United Kingdom) for 24 h at 37 °C in a shaking incubator (IKA KS 3000 ic) set at 100 rpm. The surface to volume ratio for all samples was 87.5 mm^2/ml. Indirect cytotoxicity tests were performed using serial dilutions of the extracts (100 %, 50 %, 25 %, and 12.5 %). Two samples of each type were tested. MG-63 cells were seeded in a 96-well plate at a density of 2×10^4 cells/ml. After 24 h, the medium was replaced with the extracts from materials incubations at the specified dilutions, and the cells were incubated for another 24 h. Four replicates were conducted for each sample. The next step involved assessing metabolic activity using CellTiter-Blue® Assay (Promega). The medium containing the sample extracts was replaced with 80 μl of fresh medium and 20 μl of CellTiter-Blue® Reagent, followed by incubation at 37 °C for 4 h. Subsequently, 100 μl from each well was transferred to a new plate, and fluorescence was measured at 560/590 nm using the GloMax Discover System (Promega) microplate reader.

3. Results and Discussion

3.1. Mg-Zn-Ca alloy

The use of zinc (Zn) and calcium (Ca) as components of Mg alloys enhanced the overall corrosion resistance by forming protective layers.

However, excessive concentrations of these elements may increase the vulnerability to pitting corrosion due to galvanic interactions. Zinc also improves specific mechanical properties and affects phase formation [33]. From the evaluation of literature, the suitable range of Zn between 0.4 wt.% to 1.8 wt.% at a constant Ca content of 0.2 wt.% to 0.5 wt.% can enhance the corrosion resistance behavior without affecting biocompatibility of alloy [34,35]. Also, the amount of Zn containing 0.5 wt.% can significantly refine the grain size of Mg-Ca system [35]. The low-alloyed Mg-Zn-Ca systems contain α-M g-grains along with strip-shaped phases of $Ca_2Mg_6Zn_3$ and Mg_2Ca located at the grain boundaries. Higher ratio of Zn/Ca leads to formation of these three phases, in which the electrochemical potential of $Ca_2Mg_6Zn_3$ is highest. Among other phases, the $Ca_2Mg_6Zn_3$ significantly acts as a temporary local corrosion barrier against the corrosion attack of matrix [33,36]. Considering these factors Mg-0.5Zn-0.2Ca composition is chosen for analysis. The spectrometer confirmed the elements present in the alloy, showing the following composition (weight %): Mg 99.13 wt.%, Zn 0.51 wt.% and, Ca 0.23 wt.%. Furthermore, the SEM image of the alloy is displayed in Fig. 2(a); no apparent corrosion cracks are present, however scratches from mechanical polishing are visible. Fig. 2(b) illustrates the EDS spectra of the corresponding as-cast Mg-0.5Zn-0.2Ca alloy. The chemical composition of the alloy was confirmed by EDS, indicating the presence of magnesium, zinc, and calcium. The minor presence of oxygen suggests that the material used for film deposition was not corroded. The corresponding chemical maps are demonstrated in Fig. 2 (c, d, e and f), represent the distribution of O, Mg, Ca, and Zn respectively.

3.2. *a-C:N film – morphology and characteristics*

The SEM image in Fig. 3(a) reveals the homogeneous distribution and persistence of the film across the surface before immersion in PBS solution. It is evident that the film remained intact, with a uniform distribution over the surface. The EDS analysis of the coated sample, shown in Fig. 3(b), indicates the presence of carbon, oxygen, and nitrogen on the coated magnesium alloy substrate, confirming the deposition of a protective anticorrosion film on the magnesium surface. The AFM image of the deposited a-C:N film on p-doped conductive silicon (Si) wafer is shown in inset Fig. 3(c). The thickness of the ultrathin film was examined by scratching the a-C:N thin film layer. Hight profile of scratched film shows that the average thickness of the film is approximately 34 nm. Additionally, Raman spectroscopy was conducted to get a more comprehensive understanding of the vibrational modes of the as-synthesized film. As shown in Fig. 3(d) peak corresponding to 1344 cm^{-1} indicates the "disorder" D mode [37] of sp^3 containing carbon network with A_{1g} symmetry [38] and the peak corresponding to 1578 cm^{-1} indicates "crystalline" G mode with E_{2g} symmetry [37] of sp^2 containing carbon network [39]. Furthermore, X-ray diffraction study was performed to investigate the phase structure of the as-synthesized film. Fig. S1 (Supporting Information) revealed only a broad diffraction peak at~24°, indicates amorphous phase [40] of the carbon (200) plane [41] as well as small particle size of the film [42]. TEM results of the a-C:N film displays amorphous nature accompanied by the selected-area electron diffraction (SAED) pattern. The emergence of more curved multilayer structure in Fig. 3(e) indicates the presence of the sp^2-C, which supports XPS and Raman results [43]. The SAED image in Fig. 3(f) contains diffused ring patterns which further proves the amorphous nature of a-C:N film [26].

To further confirm the elemental composition and reveal the chemical states, the a-C:N films were analyzed by XPS before corrosion. Fig. 4a shows the survey scan of a-C:N film deposited on silicon wafer. The acquired XPS survey scan indicates photo-emission signals originates from carbon, nitrogen, oxygen and silicon.

The detailed information about the chemical states of C, N, O and Si was gained by registered high-resolution spectra. The curve-fitting high-resolution spectra acquired in C 1 s, N 1 s, O 1 s and Si 2p region are shown in Fig. 4(b–e). The C 1 s spectrum (Fig. 4(b)) of the sample was fitted with four components. The first line at 285.0 eV indicates aliphatic carbon C—C [44], second line at 286.3 eV is attributed to the existence of either C—N (pyrrolic nitrogen) and/or C—O—C bonds [45], third line observed at 287.5 eV indicates presence of C═O bonds [46] and fourth line centered at 288.8 eV represents N— (C═O) (pyridinic nitrogen) type groups [44,45]. The N 1 s region (Fig. 4(c)), was fitted with two components lies at 399.2 eV which corresponds to ═N-C bonds and at 400.8 eV originates from ═══N-(C═O) bonds [47]. As shown in Fig. 4 (d), the O 1 s spectrum was fitted with two lines. The first line at 532.1 eV is associated with O═C and/or ═══N-(C═O)-N bonds [48], the second line observed at 533.6 eV can originate either O-C and/or ═-OHtype bonds and/or adsorbed water [44,45]. The Si 2p spectra (Fig. 4(e)) shown one doublet structure with $2p_{3/2}$ – $2p_{1/2}$ spin–orbit splitting equal to 0.6 eV. The first main $2p_{3/2}$ line observed at 102.2 eV is

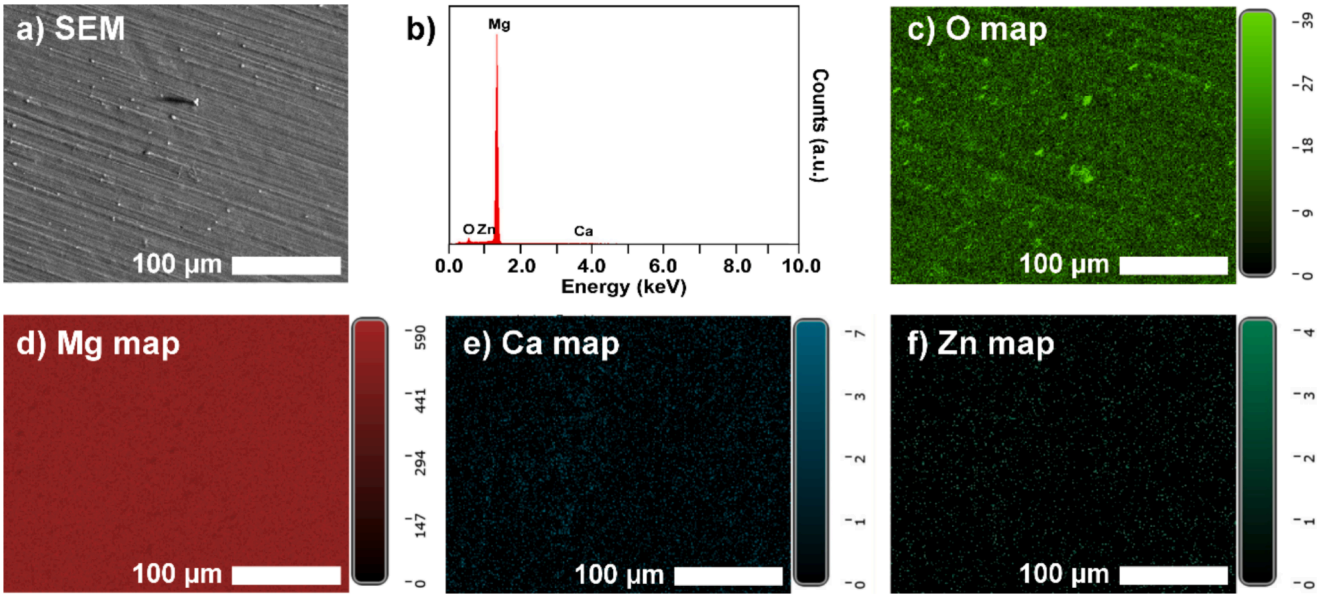

Fig. 2. (a) SEM image of the Mg alloy before coating, (b) corresponding EDS spectrum of Mg alloy indicating the presence of O, Mg, Zn and Ca (c, d, e and f) chemical maps showing the distribution of O, Mg, Ca, and Zn, respectively.

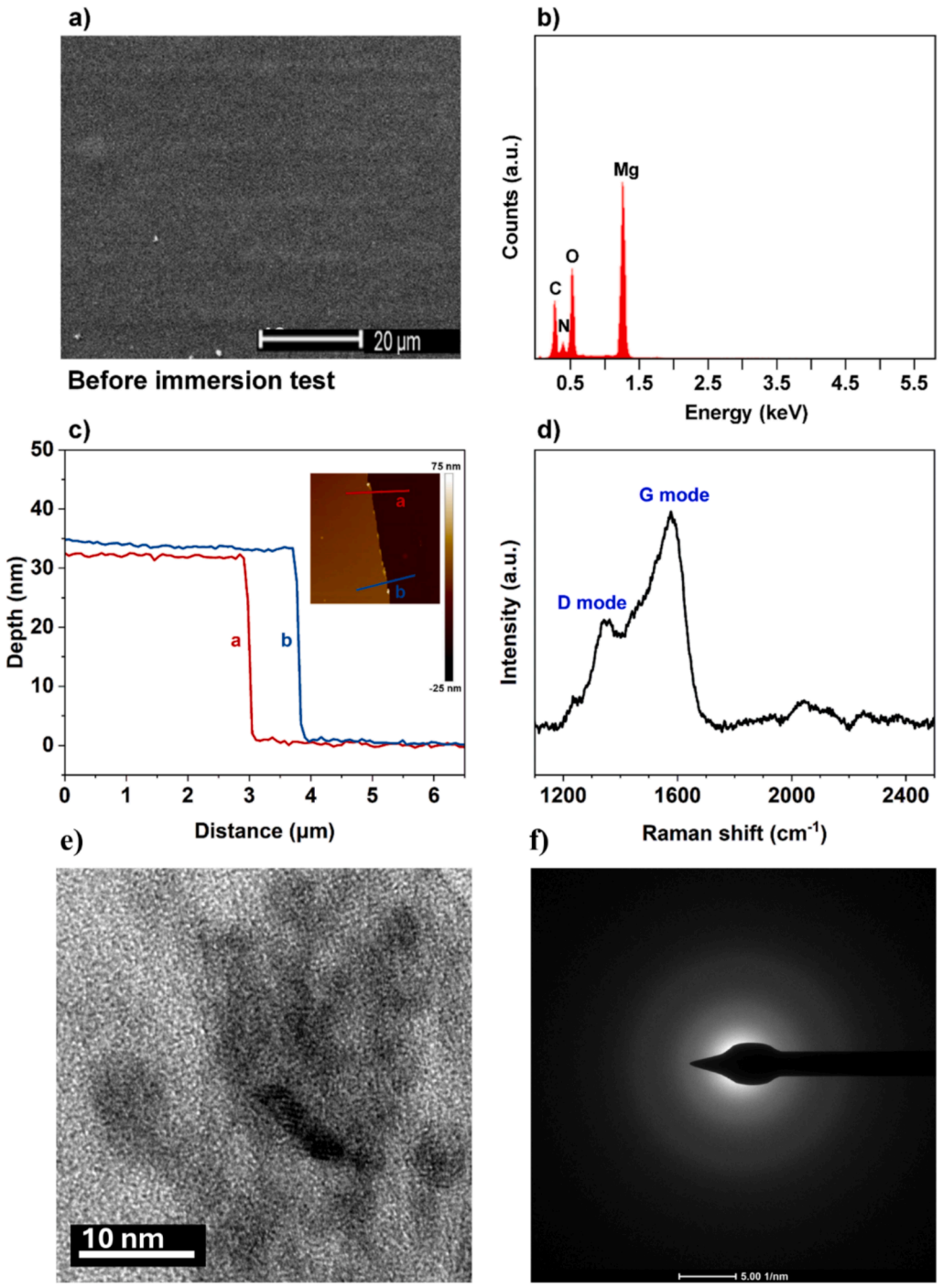

Fig. 3. Morphological characterization of the a-C:N film coated alloy before immersion test: (a) SEM image of the a-C:N film coated sample before immersion test, (b) corresponding EDS spectrum of the a-C:N film coated surface, (c) height profile of the scratched film surface; the inset shows the scratched film surface used for thickness measurements, (d) Raman spectra showing the characteristic D mode and G mode of the of a-C:N thin film, (e) HRTEM image of a-C:N film, (f) SAED containing diffused ring pattern further proves amorphous nature of the film.

related to ==C-Si-O type bonds like in siloxane or silicone compounds [48]. Thus, the detected Si 2p signal represents surface contamination probably related to the presence of Si evaporated from the silicone-based top layer of the tape that was utilized for sample preparation. The XPS analysis did not reveal any other impurities or signals from the silica substrate, which indicates that the synthesized film is continuous.

Additionally, we recorded the XPS spectrum of the a-C:N film on the targeted Mg substrate. It was found that the N 1 s peak in a-C:N layer on the Mg substrate shifted by 0.95 eV compared to the Si substrate, as shown in Fig. 5(a). In case of O 1 s peaks, a shift of 0.35 eV was observed, as shown in Fig. 5(b). This clearly indicates that functionalized pyridinic and pyrrolic nitrogen present in the film acts as a ligand, donating electrons to Mg and forming coordination bonds. Since nitrogen is a Lewis base, it interacts strongly with Lewis acids like Mg^{+2}, helping to bind the a-C:N film to the Mg substrate. Furthermore, figure S2 (Supporting Information) presents the FTIR spectrum, which confirms the presence of pyridinic nitrogen, with a peak associated with C—N stretching at 1155 cm^{-1} [49]. It was reported that the use of amorphous carbon can result in better adhesion between film and metal. However, nitrogen doping can increase in sp^2 bond fractions, which further can

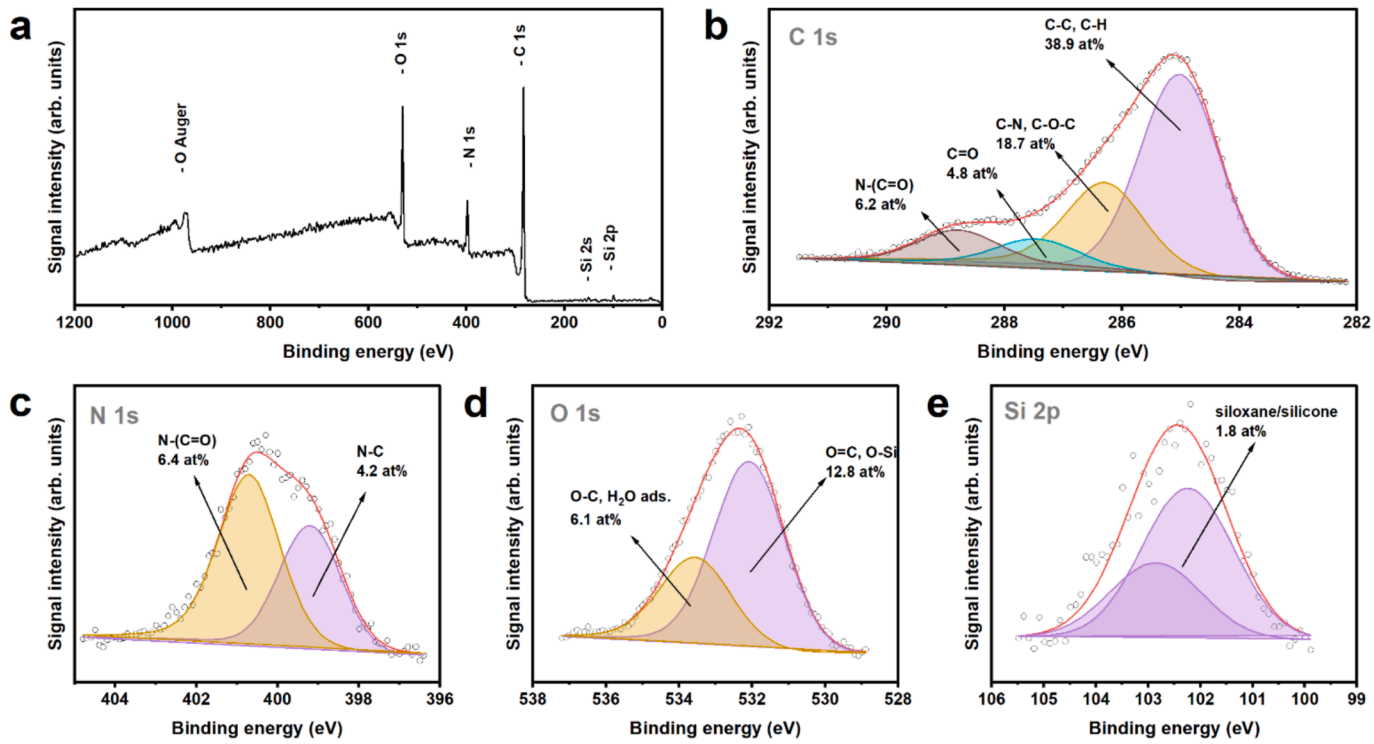

Fig. 4. XPS survey scan (a) and high-resolution spectra in (b) C 1 s, (c) N 1 s (d) O 1 s (e) Si 2p region for the a-C:N film covered Si wafer.

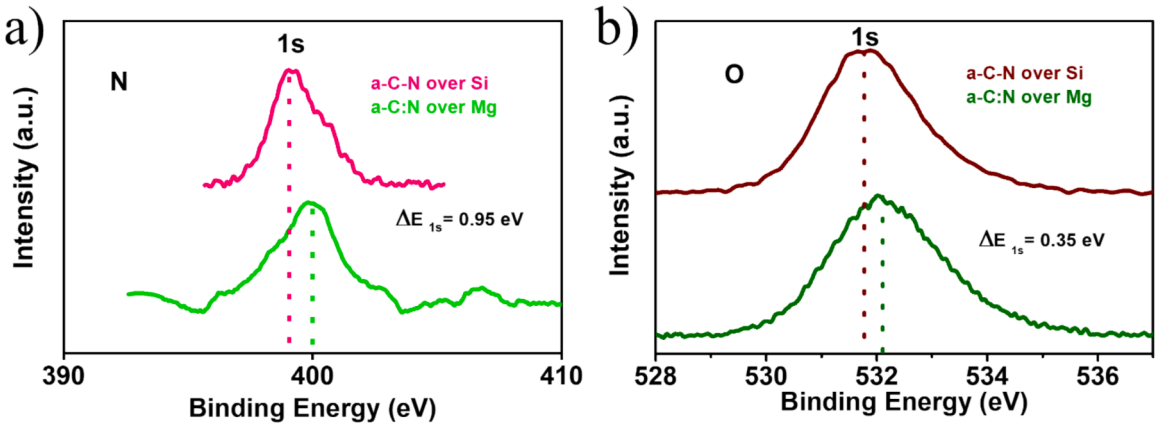

Fig. 5. Core level compared XPS spectra of (a) N 1 s from the a-C:N film on the Mg alloy and p++Si substrate and (b) O 1 s for the a-C:N film on the Mg alloy and p++Si substrate.

increase the surface energy and reduces residual stress within the film which ultimately contributes better adhesion [50,51]. Specifically, nitrogen content in the film enhances the clustering of sp^2 sites because of preferential π bonding of nitrogen [51]. The presence of nitrogen content in a-C:N film contributes to the formation of C═N bonds with shorter bond lengths than C═C or C—C bonds, which leads to reduction in strain within the film [52]. Overall, nitrogen doping lowers the internal stress and strain in the film, resulting in improved adhesion, film toughness and reduces hardness. Moreover, nitrogen has a better donor capability than oxygen and thus interacts more efficiently with Lewis acid Mg^{2+} ions in the substrate, further enhancing adhesion between the film and substrate both before and after immersion [53]. Several methods for preparing a-C:N films, such as incorporating graphene [32], using nitrogen doped DLC coatings [23], and utilizing polymer based coatings [26], have demonstrated better adhesion between films and surface. For instance, a-C:N film synthesized by using branched polyethyleneimine and glucose have exhibited very good adhesion, remaining firmly attached to the substrate even after multiple folding cycles. [26]. In this study, the composition obtained from XPS after corrosion in PBS solution shows the presence of the film over the surface of the alloy, which further proves the positive interaction between the film and substrate, as discussed in the later section (3.3 corrosion tests).

3.3. Corrosion tests

Morphology after immersion in HCl and PBS solution

Fig. 6 and figure S3 (supporting information) show a detailed analysis using atomic force microscopy (AFM) to examine the surface morphology of a-C:N thin films and any changes resulting from exposure to a corrosive environment. The a-C:N thin films deposited on p-doped conductive silicon (Si) wafers were submerged in a dilute hydrochloric acid solution (pH 6.9) for a duration of 24 h each. As shown in Fig. 6, for a range of 2 μm, the average roughness of the film was measured at 0.347 ± 0.009 prior to immersion, increasing slightly to 0.375 ± 0.006

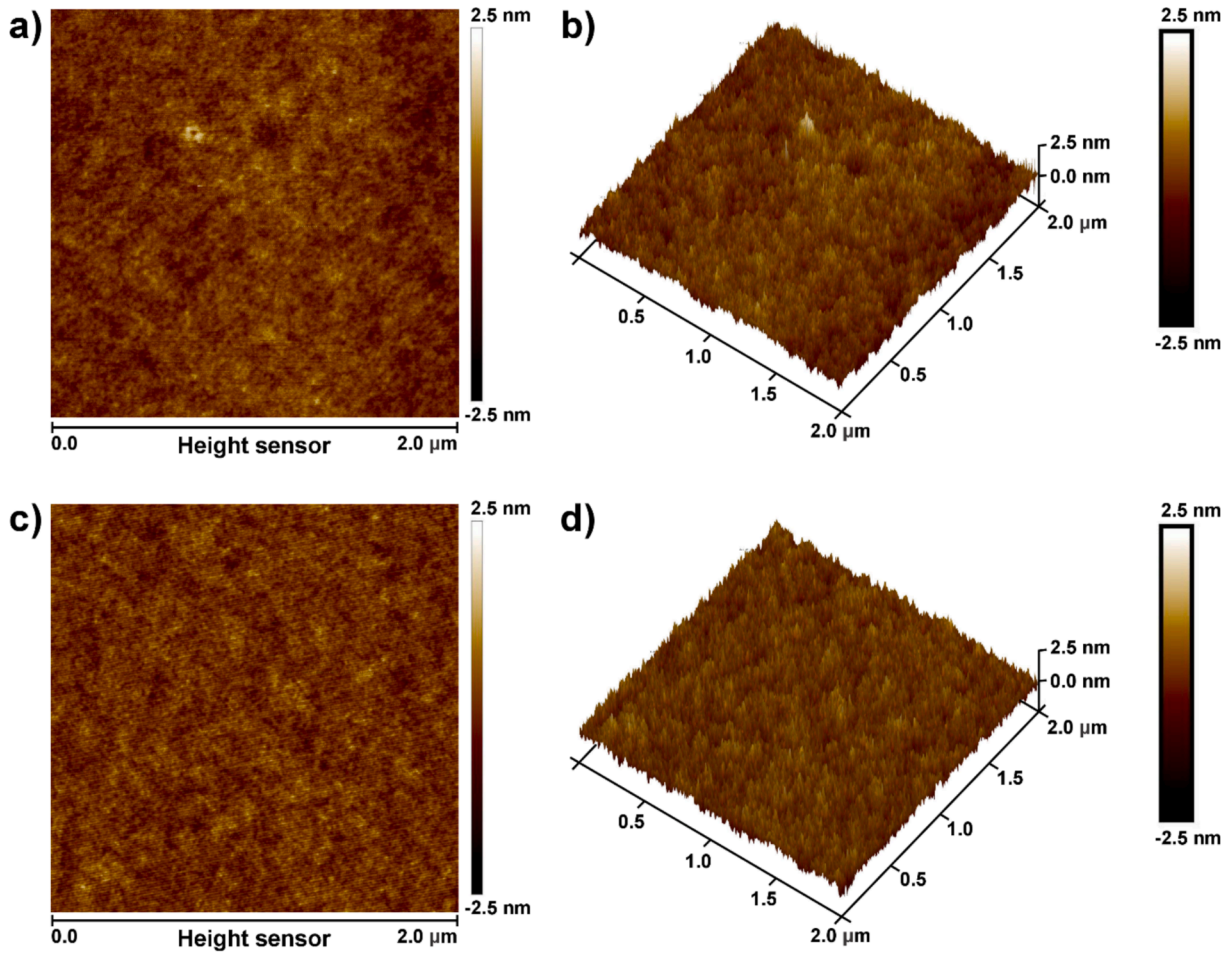

Fig. 6. Surface microstructure: 2-D cross sectional image of the a-C:N thin film (a) before and (c) after immersion in dilute HCl (pH 6.9) for 24 h. 3-D cross sectional image of the a-C:N thin film (b) before and (d) after immersion.

afterward. As shown in figure S3 (supporting information), for a range of 10 µm, the average roughness was 0.330 ± 0.012 before immersion and 0.381 ± 0.010 after. This minor change suggests that the rate of degradation or corrosion is negligible. In general, the smooth or flat film surface contributes better corrosion resistance, however, this is not only the sole factor for understanding corrosion resistance [20]. Additionally, 2-D cross-sectional images taken before immersion (Fig. 6 (a) and Fig. S3 (a)) and after immersion (Fig. 6 (c) and Fig. S3(c)) did not show any significant alterations in the film structure. Similarly, three-dimensional images captured before immersion (Fig. 6 (b) and Fig. S3(b)) and after immersion (Fig. 6 (d) and Fig. S3(d)) also indicated no notable changes took place. Collectively, these results reinforce the conclusion that the a-C:N thin films demonstrate an exceptionally low corrosion rate, highlighting their stability and durability under corrosive conditions.

The changes in the chemical states of a-C:N films after EIS tests in PBS solution were also studied by XPS. The elemental composition was revealed by a survey scan, as shown in Fig. 7(a). As can be seen from Fig. 7(a), the acquired scan for the a-C:N film deposited on the Mg alloy reveals signals from C, O, N, and Si, which are part of the film composition, along with signals from Mg and other elements due to immersion in PBS. The detected Na and Cl ions came from PBS, while Mg from the substrate. All detected elements were further analyzed in terms of chemical states by using high-resolution spectra registered in the C 1 s, N 1 s, O 1 s, Si 2p, Mg 1 s, Na 1 s and Cl 2p regions, as shown in Fig. 7.

The C 1 s, N 1 s, O 1 s and Si 2p spectra were fitted in the same manner as for the film before immersion (shown in Fig. 4), indicating that no new bonds were formed involving these elements. However, after immersion, the concentration of aliphatic C—C carbon increased (from 38.9 at.% to 41.7 at.%), while the concentration of N-containing functional groups, such as pyrrolic nitrogen (from 4.2 at.% to 1.9 at.%) and pyridinic nitrogen (from 6.4 at.% to 4.3 at.%), decreased. These changes are not significant and can be explained by the formation of a carbon residue after contact with the medium and drying of the sample, which covers the signals coming from nitrogen atoms. Signals from magnesium, sodium and chlorine were detected only in the film after corrosion. The Mg 1 s spectrum was fitted with a single line centered at 1304.3 eV which indicates presence of Mg^{2+} ions oxidation state in either oxides or chlorides [54].

It is worth emphasizing that the concentration of Mg^{2+} ions is trace (0.8 at.%) and may result from the disruption of the a-C:N film, followed by the corrosion of the substrate. The Na 1 s spectrum was fitted with single line centered at 1071.6 eV which indicates Na^{+} oxidation state of sodium [54]. The Cl 2p spectrum was fitted with doublet structure (doublet separation $2p_{3/2} - 2p_{1/2}$ equals 1.6 eV) with the main $2p_{3/2}$ line centered at 198.2 eV which indicate presence of Cl^{-} ions in chlorides like $MgCl_2$ [54]. The XPS analysis shows that the synthesized a-C:N film does not corrode, i.e. its chemistry does not change significantly after immersion in PBS.

Fig. 8(a) examines a corroded sample after 7 days of immersion in dilute HCl (pH 6.9). The SEM image indicates that the sample experienced corrosion, resulting in a more discontinuous film. The uneven distribution of elements is likely due to localized corrosion, which leads to the formation of a mineral layer. This mineral layer is not uniformly distributed across the film surface, resulting in a discontinuous film. However, the advantage of this layer is that it is distributed across the surface of the nanofilm, further serving as a corrosion barrier [55]. The

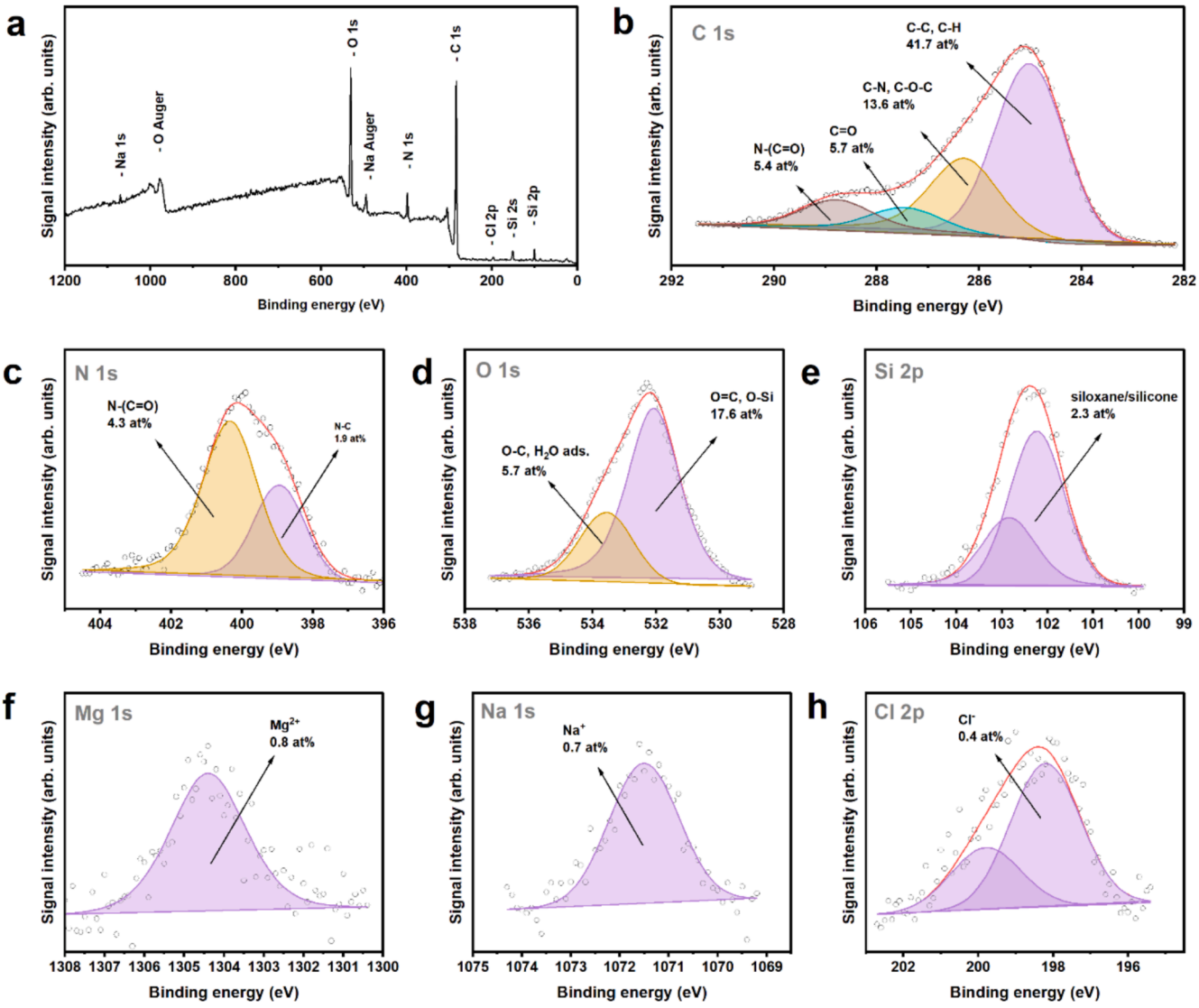

Fig. 7. (a) XPS survey scan and high-resolution XPS spectra in the (b) C 1 s, (c) N 1 s, (d) O 1 s. (e) Si 2p, (f) Mg 1 s, (g) Na 1 s and (h) Cl 2p region for the a-C:N film covered Mg alloy after an hour in PBS.

EDS spectrum in figure S4 (supporting information) confirmed the presence of oxygen in addition to the typical alloy components. Fig. 8 (b)−(f), display the corresponding chemical maps, indicating the presence and distribution of carbon, nitrogen, chlorine, oxygen and magnesium, respectively. In Fig. 9, the uncoated and a-C:N film deposited on the alloy surface was examined after immersion in the phosphate buffered saline (PBS) solution. The a-C:N thin film demonstrated strong adhesion to the underlying substrate, with no signs of delamination or peeling even after repeated washing with water and ethanol. Furthermore, the a-C:N coating maintained its adhesion even when applied on rough or uneven surfaces. To investigate the differences in the corrosion rate, we analyzed the morphology of the coated sample after immersion in PBS solution for 3 days. Following immersion, the uncoated sample exhibited a rapid rate of corrosion, as seen in Fig. 9(a). In contrast, Fig. 9 (b) and (c) show negligible corrosion cracks on the surface of the coating, with the film maintaining adhesion to the substrate throughout this period. During three days of immersion, Fig. 9(a) depicts the development of apparent mineral layers on the magnesium surface. These layers would increase the substrate resistance to corrosion, leading to slower rates of corrosion during extended immersion. However, given their multilayer nature, it is likely that the extensive defects and poor adherence of these loosely packed sediments prevented them from offering the substrate enough protection. The corrosion behavior of coated surface was more complicated than that of uncoated sample. Due to the a-C:N film hydrolysis and dissolution during immersion testing, only minor defects were found in coating covering. The film contains oxygen in a form of C=O bonds, contributing to electrostatic attraction between the film and the magnesium substrate, indicating strong adhesion [55]. The minor defects observed after immersion are likely due to the hydrolysis of the film and the release of hydrogen bubbles caused by oxidation of the magnesium substrate [16,55]. In this case, the oxidation of magnesium is relatively slow, leading to a low rate of hydrogen evolution. However, the rapid accumulation of corrosion products, particularly hydrogen bubbles, can still potentially damage the coatings. Due to the relatively thin nature of the film, water molecules can permeate through the small pores within the coating, which may facilitate the expulsion of the hydrogen bubbles formed during the corrosion process. Additionally, SEM images (in Figs. 8 and 9) confirmed the presence of mineral deposits embedded within the film. These film-mineral composites positively impact the long-term performance and durability of the coating, as the formation of these film-mineral composites helps prevent the detachment or shedding of the mineral components. The interaction between the film and the mineral phases enhances overall corrosion resistance [55–58]. Unlike previous

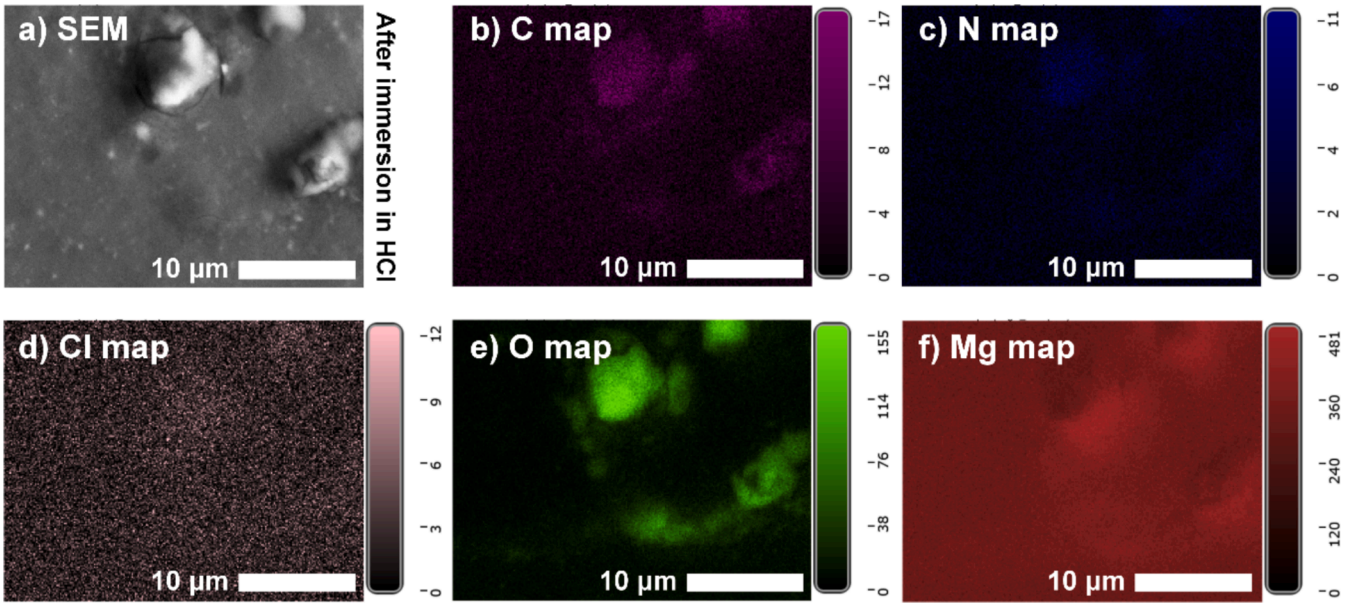

Fig. 8. (a) SEM image of the coated alloy after 7 days of immersion in dilute HCl (pH 6.9), with (b) to (f) showing chemical maps of carbon, nitrogen, chlorine, oxygen, and magnesium, respectively.

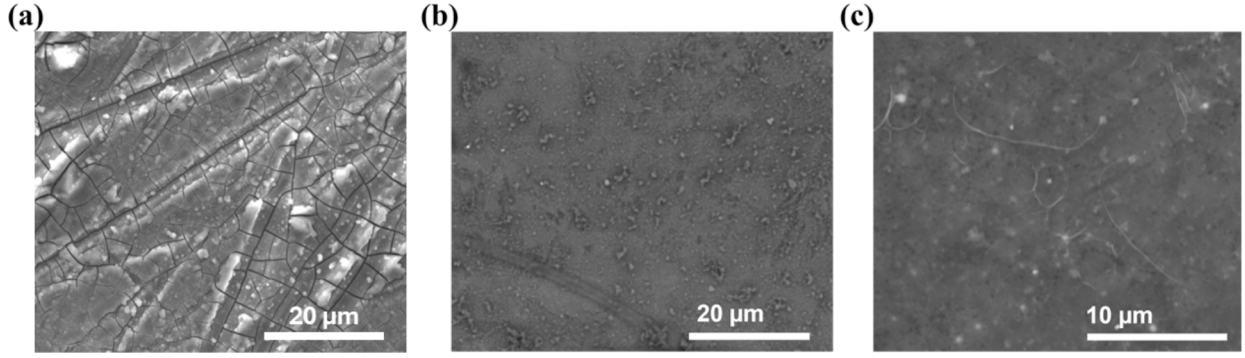

Fig. 9. SEM image of (a) uncoated and (b, c) coated Mg alloy after 3 days immersion in PBS solution.

observations, no peeling or delamination of the other coating films was noted during immersion in PBS solution, even after 3-days soaking period. Although minor defects and the presence of mineral deposits were observed on these coatings, the films remained firmly adhered to the substrate without any signs of detachment. The robust and stable nature of the protective coating contributed to significantly lower corrosion rates of the underlying substrate. This multifaceted mechanism involves several key processes: substrate corrosion, hydrolysis (breakdown) of the polymeric components in the coating, and the subsequent formation of polymer-mineral composite structures. These

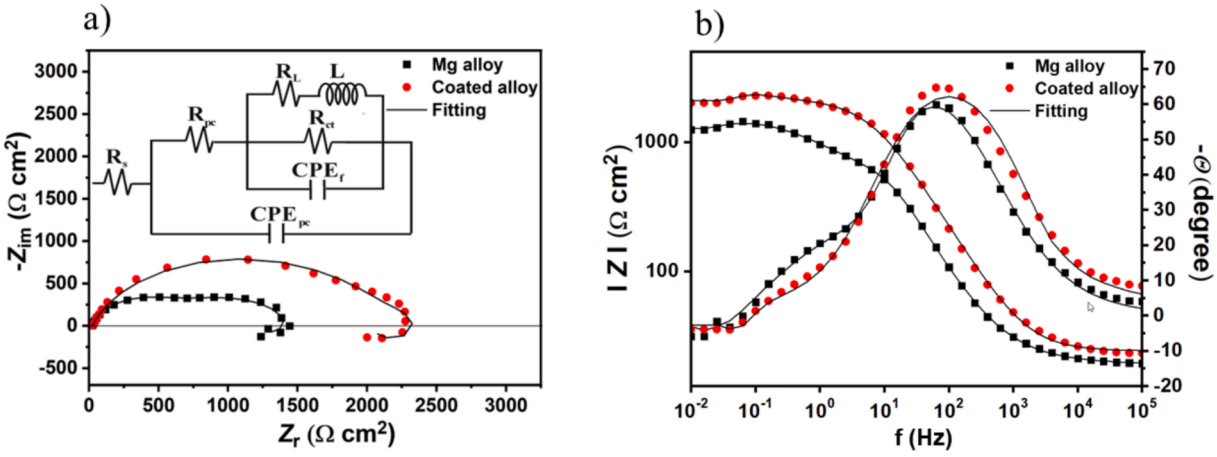

Fig. 10. (a) Nyquist and (b) Bode plots of the Mg alloy and coated alloy.

findings strongly suggest that the film coatings not only provide initial protection but also actively contribute to the generation of these polymer-mineral composites. The formation of these composite structures has the potential to further enhance the long-term corrosion resistance of the coated system. As a result, the coated sample exhibited a remarkably low corrosion rate, even after extended immersion periods.

Electrochemical corrosion tests.

Fig. 10 depicts the Nyquist and Bode plots for the substrate and coated sample. The EIS plots show the presence of three-time constants on both coated and free-coated substrate, namely, two capacitive loops at high and medium frequencies (HF and MF, respectively), followed by an inductive loop at low frequencies (LF), in agreement with data reported in the literature for Mg alloy [20,23,25,59–62]. The capacitive loop at HF has been associated with the charge transfer (electron transfer) and electrochemical double-layer and barrier film effects. The MF-frequency arc has been associated with mass transfer relaxation in protective oxide films. Finally, the inductive loop at LF has been related to the presence of relaxation of processes due to the adsorption of species at the corrosion layer and/or pitting corrosion initiation [63].

To understand the electrochemical corrosion mechanism of the Mg alloy and coated substrate, the EIS plots were fitted according to the electrical equivalent circuits (EEC) [20,23,25,59–62] model shown in Fig. 10(a) (inset), and the fitting results are listed in Table 1. R_s represents the solution resistance, R_{cp} and R_{ct} represent the resistance of the corrosion products layer on the substrate surface and charge transfer resistance, respectively, CPE_{cp} and CPE_f are associated with the corrosion area of the electrode and the coating thickness on the substrate surface, respectively. The constant phase element (CPE) was used in the EEC as a replacement for the capacitance to account for the non-homogeneity nature of the electrode surface and is composed of two elements, Q and n; Q is caused by the dispersion effect through defects, etc., and n is the dispersion index which varies from 0 to 1. Higher values of n imply that the CPE behaves as a capacitor, whereas lower values suggest rougher surfaces with higher coating porosity [23,25]. Lastly, L and R_L represent the inductance and the resistance of the passivation film formed through pitting [23,25]. $\chi 2$ values were approximately 10^{-3}, suggesting that the EEC proposed was consistent with the corrosion phenomenon on the Mg alloy and coated substrate in PBS solution.

According to the literature [23,25,62], two different layers are formed on the Mg alloy surface: a thin barrier layer of MgO, formed as soon as the metal is immersed in the PBS solution, followed by a thicker porous layer of $Mg(OH)_2$ coating the MgO layer. The high-frequency capacitive arc is due to the charge-transfer resistance of anodic and cathodic reactions (Eqs. (1) and (2)) [62]. The newly formed Mg^{2+} ions react with the OH^- anions to form a $Mg(OH)_2$ layer (Eq. (3)) [63]. The overall degradation of Mg alloys in a water-based solution can be depicted using (Eq. (4)) [23,25,63].

$$Mg \rightarrow Mg^{2+} + 2e^- \quad (1)$$

$$2H_2O + 2e^- \rightarrow H_2 + OH^- \quad (2)$$

$$Mg^{2+} + OH^- \rightarrow Mg(OH)_2 \quad (3)$$

$$Mg + 2H_2O \rightarrow Mg(OH)_2 + H_2 \quad (4)$$

However, $Mg(OH)_2$ is unstable in environments with chloride ions concentration exceeding 30 mM, allowing the solution to diffuse through it and react with the substrate [25]. In PBS neutral solution, the chloride ions concentration is around 0.14 M [64–66], leading to the outer layer's rapid deterioration. In this situation, Mg dissolved in the film-free areas, and the Mg^{2+} ions formed and then diffused through the porous $Mg(OH)_2$ layer, generating the second capacitance loop observed in the EIS plots at MF [62]. Conversely, as shown in Fig. 10 (a and b), with the application of the coating on the Mg alloy, the arc at the HF range increases, and the maximum phase angle peak and peak width are larger than the free-coating substrate. As can be seen from Table 1, the charge transfer for the coated substrate is bigger than the free-coated Mg alloy, denoting that the corrosion processes at the substrate are hindered by the coating, which, in turn, also leads to the decrease of the capacitive loop at MF.

The potentiodynamic polarization curves of the substrate and the coated sample immersed in PBS are shown in Fig. 11, and the electrochemical parameters obtained through the Tafel extrapolation method are listed in Table 2. The corrosion performance of a given metal mostly depends on I_{corr} values, while E_{corr} is a measure of the corrosive tendency. A smaller I_{corr} value corresponded to higher corrosion performance [67]. The results revealed that thin film coating on the magnesium alloy exhibited lower corrosion current (I_{corr}) values and more positive corrosion potential (E_{corr}) values compared to the pure Mg alloy, indicating that the coatings improve the corrosion resistance of the Mg alloy by effectively inhibiting the passage of aggressive solutions to the substrate. These results are consistent with those of the EIS measurements.

3.4. Cytotoxicity tests

Fig. 12 shows the survival rate of human osteoblast cells cultured in extracts from both the uncoated and the coated magnesium alloy samples. The data indicates no significant differences in cell survival between the materials studied. A 100 % value corresponds to control, where cells were incubated with the complete medium. In general, relative metabolic activity above 70 % is considered indicative of non-

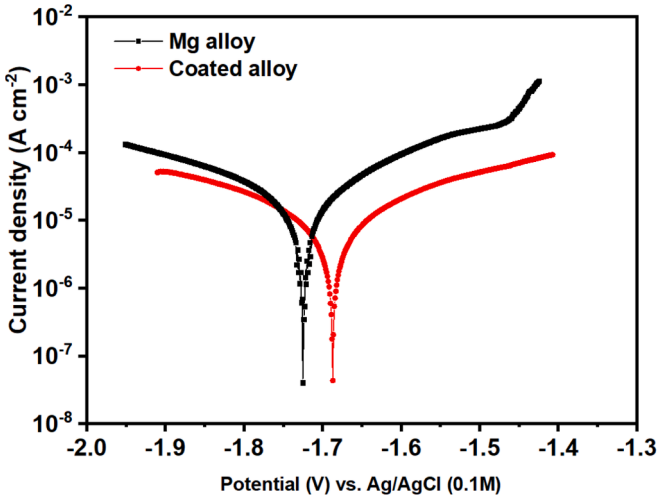

Fig. 11. Potentiodynamic polarization curves of the Mg alloy and coated alloy in PBS solution.

Table 1
EIS parameters for the Mg alloy and coated alloy in PBS solution.

Sample	R_s (Ω Cm^2)	CPE_{cp}		R_{cp} (Ω Cm^2)	CPE_f		R_{ct} (Ω Cm^2)	L (H cm^{-2})	R_L (Ω Cm^2)	$\chi 2$ (10^{-3})
		Q_{cp} (μΩ^{-1}cm^{-2} s^n)	n_{cp}		Q_f (μΩ^{-1}cm^{-2} s^n)	n_f				
Mg alloy	20.32	52.02	0.806	94.57	782.2	0.81	1320	4934	372.3	2.58
Coated alloy	21.34	14.56	0.96	671	364.5	0.89	7722	5740	1283	1.78

Table 2
Potentiodynamic polarization data of the Mg alloy and coated alloy in PBS solution.

Sample	E_{corr} (V)	β_a (V dec^{-1})	β_c (V dec^{-1})	I_{corr} (μA cm^{-2})
Mg alloy	−1.728	0.270	0.174	32.12
Coated alloy	−1.689	0.292	0.235	8.82

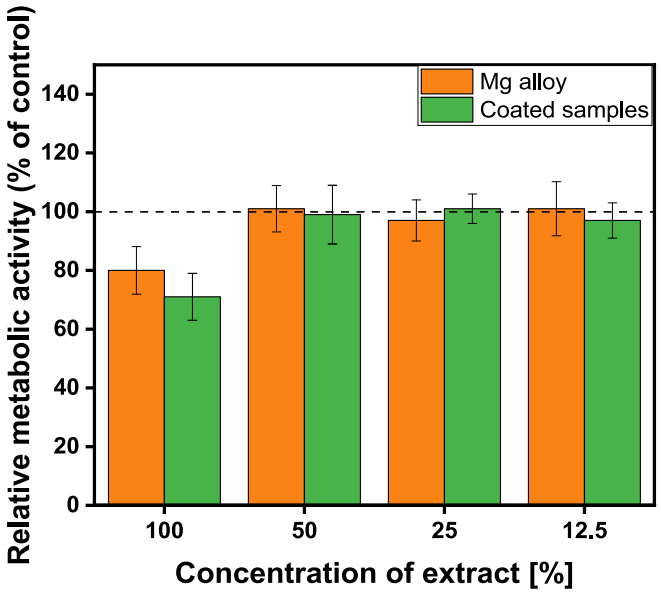

Fig. 12. The coated samples (green) and the magnesium alloy (orange) relative metabolic activity vs concentration of extract were represented. (For interpretation of the references to colour in this figure legend, the reader is referred to the web version of this article.)

toxic material [68]. In the case of the coated sample at 100 % extract concentration the value was at the threshold of non-toxicity, measuring 68.7 ± 8.1 %, while all other values were above 70 %. In case of all dilutions of extracts from both coated and uncoated alloy the cells survival was at the level of control sample indicating no stressful or cytotoxic conditions. Previous studies have also shown that non-toxic Mg-Zn-Ca alloys and a-C:N thin films are suitable for biomedical applications [69,70]. Importantly, coatings on metallic biomaterials are widely studied solution to design materials eliciting specific biological response of the attaching tissues along with improving corrosion resistance [71–73]. The indirect cytotoxicity assay is an essential initial step of biological evaluation performed for biodegradable materials, including biomedical alloys, polymers and composites. It enables to investigate if degradation products possess any significant harmful effect on cells in the *in vitro* conditions that would eliminate such material from further assessment towards biomedical applications. In this work, we confirmed that the a-C:N coating, which improves the corrosion resistance of magnesium alloys, is non-toxic. However, further in-depth biological studies are necessary to confirm the safety of both the alloy and the coating for orthopedic implants.

4. Conclusions

In this work, a-C:N thin film has been synthesized using aqueous solution of b-PEI and D-(+) glucose, mixture in 1:1 vol ratio. After the synthesis of the film, it was transferred onto the surface of Mg-0.5Zn-0.2Ca alloy. Furthermore, the influence of the nitrogen-containing a-C:N film on the surface has been studied. The effects of the a-C:N film on surface properties, such as corrosion, toxicity, morphology, and compositional changes, have also been explored. Based on this study, the following conclusions have been drawn:

(1) The synthesis process for a-C:N film involves the mixing of aqueous solution of b-PEI and glucose in 1:1 vol ratio, which is cost effective. Also, the transfer process and nitrogen concentration have been optimized by changing the concentration of b-PEI and glucose in the initial solution.
(2) The amorphous nature of the a-C:N film was further demonstrated by the HRTEM and XRD results. XPS results before and after corrosion, along with Raman spectroscopy revealed the presence of sp^2 clusters. Because nitrogen has a greater ability to donate electrons than oxygen, it may interact more effectively with the Lewis acid Mg^{2+} ions in the substrate. This interaction significantly enhances the adhesion between the film and the substrate. Additionally, it was observed that film is not delaminated from the surface even after seven days of immersion in dil. HCl solution.
(3) The electrochemical tests results demonstrated that the I_{corr} value for coating is significantly lower than that of the substrate, while the R_{pc}, R_{ct} values for coating are higher than those of the alloy, indicating that the film enhances corrosion resistance. After long-term immersion in PBS and HCl, the coated surface exhibited less degradation than the bare magnesium alloy, demonstrating exceptional corrosion resistance.
(4) Carbon, being a biocompatible and inert nonmetallic element, is an attractive choice for this application. Importantly, cytotoxicity tests revealed that the a-C:N film is non-toxic, making it a suitable candidate for orthopedic implants. However, further studies on biocompatibility can be employed for testing the a-C:N film compatibility over the surface of magnesium alloy.

Overall, this study represents the first report on the utilization of a-C:N film on the Mg-0.5Zn-0.2Ca alloy synthesized by using microwave. The film is ultrathin, ultra-smooth, and corrosion-resistant, opening new ways for the development of advanced Mg-based implants with enhanced long-term performance and improved clinical outcomes for patients.

CRediT authorship contribution statement

Adarsh Rai: Writing – original draft, Visualization, Validation, Project administration, Methodology, Investigation, Formal analysis, Conceptualization. **Mateusz Szczerba:** Writing – review & editing, Validation, Investigation. **Joanna Karbowniczek:** Writing – review & editing, Investigation. **Kamil Cichocki:** Investigation. **Michal Krzyzanowski:** Writing – review & editing, Supervision. **Szymon Bajda:** Writing – original draft, Supervision, Investigation. **Grzegorz D. Sulka:** Writing – review & editing, Supervision, Resources. **Michał Szuwarzyński:** Writing – review & editing, Investigation. **Krystian Sokołowski:** Writing – review & editing, Investigation. **Björn Wiese:** Investigation.

Declaration of competing interest

The authors declare that they have no known competing financial interests or personal relationships that could have appeared to influence the work reported in this paper.

Acknowledgements

The support from the National Science Center, Poland (grant no. 2024/53/B/ST11/00799) is greatly appreciated. Cytotoxicity evaluation was performed with financial support from the Polish Ministry of Science and Higher Education: research subvention to AGH University of Krakow no. 16.16.110.663. The authors are thankful to Dr. Gaetano Pulambo, AGH University of Krakow, for his support in corrosion

measurements.

Appendix A. Supplementary data

Supplementary data to this article can be found online at https://doi.org/10.1016/j.apsusc.2025.162847.

Data availability

Data will be made available on request.

References

[1] A. Wiese, H.C. Pape, Bone defects caused by high-energy injuries, bone loss, infected nonunions, and nonunions, Orthop Clin North Am 41 (2010) 1–4, table of contents, doi: 10.1016/j.ocl.2009.07.003.

[2] V.M. Goldberg, J.A. Buckwalter, W.C. Hayes, K.J. Koval, Orthopaedic challenges in an aging population, INSTRUCTIONAL COURSE LECTURES-AMERICAN ACADEMY OF ORTHOPAEDIC SURGEONS 46 (1997) 417–422.

[3] A. Le Moine, M. Goldman, D. Abramowicz, Multiple pathways to allograft rejection, Transplantation 73 (2002) 1373, https://doi.org/10.1097/00007890-200205150-00001.

[4] S. Nilawar, M. Uddin, K. Chatterjee, Surface engineering of biodegradable implants: emerging trends in bioactive ceramic coatings and mechanical treatments, Mater. Adv. 2 (2021) 7820–7841, https://doi.org/10.1039/D1MA00733E.

[5] O. Böstman, H. Pihlajamäki, Clinical biocompatibility of biodegradable orthopaedic implants for internal fixation: a review, Biomaterials 21 (2000) 2615–2621, https://doi.org/10.1016/S0142-9612(00)00129-0.

[6] F.A. Barber, W.D. Dockery, Long-term absorption of poly-L-lactic acid interference screws, Arthroscopy 22 (2006) 820–826, https://doi.org/10.1016/j.arthro.2006.04.096.

[7] B.L. Mordike, T. Ebert, Magnesium: Properties — applications — potential, Mater. Sci. Eng. A 302 (2001) 37–45, https://doi.org/10.1016/S0921-5093(00)01351-4.

[8] D. Zhao, F. Witte, F. Lu, J. Wang, J. Li, L. Qin, Current status on clinical applications of magnesium-based orthopaedic implants: a review from clinical translational perspective, Biomaterials 112 (2017) 287–302, https://doi.org/10.1016/j.biomaterials.2016.10.017.

[9] M.P. Staiger, A.M. Pietak, J. Huadmai, G. Dias, Magnesium and its alloys as orthopedic biomaterials: a review, Biomaterials 27 (2006) 1728–1734, https://doi.org/10.1016/j.biomaterials.2005.10.003.

[10] F. Witte, V. Kaese, H. Haferkamp, E. Switzer, A. Meyer-Lindenberg, C.J. Wirth, H. Windhagen, In vivo corrosion of four magnesium alloys and the associated bone response, Biomaterials 26 (2005) 3557–3563, https://doi.org/10.1016/j.biomaterials.2004.09.049.

[11] C. Castellani, R.A. Lindtner, P. Hausbrandt, E. Tschegg, S.E. Stanzl-Tschegg, G. Zanoni, S. Beck, A.-M. Weinberg, Bone-implant interface strength and osseointegration: biodegradable magnesium alloy versus standard titanium control, Acta Biomater 7 (2011) 432–440, https://doi.org/10.1016/j.actbio.2010.08.020.

[12] G. Baril, N. Pébère, The corrosion of pure magnesium in aerated and deaerated sodium sulphate solutions, Corros. Sci. 43 (2001) 471–484, https://doi.org/10.1016/S0010-938X(00)00095-0.

[13] F. Witte, The history of biodegradable magnesium implants: a review, Acta Biomater. 6 (2010) 1680–1692, https://doi.org/10.1016/j.actbio.2010.02.028.

[14] J. Chen, J. Wang, E. Han, J. Dong, W. Ke, States and transport of hydrogen in the corrosion process of an AZ91 magnesium alloy in aqueous solution, Corros. Sci. 50 (2008) 1292–1305, https://doi.org/10.1016/j.corsci.2008.01.028.

[15] L. Wei, Z. Gao, Recent research advances on corrosion mechanism and protection, and novel coating materials of magnesium alloys: a review, RSC Adv. 13 (2023) 8427–8463, https://doi.org/10.1039/D2RA07829E.

[16] M. Esmaily, J.E. Svensson, S. Fajardo, N. Birbilis, G.S. Frankel, S. Virtanen, R. Arrabal, S. Thomas, L.G. Johansson, Fundamentals and advances in magnesium alloy corrosion, Prog. Mater Sci. 89 (2017) 92–193, https://doi.org/10.1016/j.pmatsci.2017.04.011.

[17] H.M. Wong, K.W.K. Yeung, K.O. Lam, V. Tam, P.K. Chu, K.D.K. Luk, K.M. C. Cheung, A biodegradable polymer-based coating to control the performance of magnesium alloy orthopaedic implants, Biomaterials 31 (2010) 2084–2096, https://doi.org/10.1016/j.biomaterials.2009.11.111.

[18] J.N. Li, P. Cao, X.N. Zhang, S.X. Zhang, Y.H. He, In vitro degradation and cell attachment of a PLGA coated biodegradable Mg–6Zn based alloy, J Mater Sci 45 (2010) 6038–6045, https://doi.org/10.1007/s10853-010-4688-9.

[19] L. Xu, A. Yamamoto, Characteristics and cytocompatibility of biodegradable polymer film on magnesium by spin coating, Colloids Surf. B Biointerfaces 93 (2012) 67–74, https://doi.org/10.1016/j.colsurfb.2011.12.009.

[20] L. Li, Z. Zhang, D. Zhang, F. Qi, Y. Dai, W. Wei, X. Ouyang, Effects of metal ion implantation (Fe, Ti, Zn and Zr) on mechanical properties, corrosion resistance and biocompatibility of WE43 Mg alloy, J. Magnesium Alloys 13 (2025) 296–310, https://doi.org/10.1016/j.jma.2024.05.005.

[21] W. Yao, Y. Tan, Q. Lu, H. Yi, C. Cheng, L. Wu, V.S. Saji, F. Pan, Recent advances in protective coatings and surface modifications for corrosion protection of Mg alloys, J. Mater. Res. Technol. 31 (2024) 3238–3254, https://doi.org/10.1016/j.jmrt.2024.07.046.

[22] H. Cao, H. Li, F. Liu, W. Luo, F. Qi, N. Zhao, X. Ouyang, B. Liao, Microstructure, mechanical and tribological properties of multilayer TiAl/TiAlN coatings on Al alloys by FCVA technology, Ceram. Int. 48 (2022) 5476–5487, https://doi.org/10.1016/j.ceramint.2021.11.092.

[23] Z. Xiao, L. Ren, C. Guo, L. Liang, Y. Dai, K. Tang, L. Lu, F. Qi, J. She, L. Wang, X. Ouyang, Enhanced corrosion resistance, mechanical properties, and biocompatibility of N-DLC coatings prepared on WE43 alloy via FCVA technology, J. Alloy. Compd. 1010 (2025) 178106, https://doi.org/10.1016/j.jallcom.2024.178106.

[24] A. Anders, Approaches to rid cathodic arc plasmas of macro- and nanoparticles: a review, Surf. Coat. Technol. 120–121 (1999) 319–330, https://doi.org/10.1016/S0257-8972(99)00460-0.

[25] L. Ren, X. Liu, H. Cao, Y. Tang, F. Qi, N. Zhao, Y. Dai, X. Ouyang, Mechanical and corrosion properties of hydrogen-free DLC coatings prepared on degradable as-extruded WE43 alloy using FCVA technology, Surf. Coat. Technol. 476 (2024) 130293, https://doi.org/10.1016/j.surfcoat.2023.130293.

[26] M. Pal, A. Giri, D.W. Kim, S. Shin, M. Kong, K. Thiyagarajan, J. Kwak, O.F. N. Okello, S.-Y. Choi, U. Jeong, Fabrication of foldable metal interconnections by hybridizing with amorphous carbon ultrathin anisotropic conductive film, ACS Nano 13 (2019) 7175–7184, https://doi.org/10.1021/acsnano.9b02649.

[27] S. Saha, R. Sinha, R. Hatada, W. Ensinger, S. Flege, K. Baba, A.K. Meikap, Effect of doping and preparation parameter on AC conductivity and dielectric modulus formalism of Al doped DLC thin films, Diam. Relat. Mater. 146 (2024) 111193, https://doi.org/10.1016/j.diamond.2024.111193.

[28] M. Zhao, D. Li, Y. Zhang, M. Guo, X. Deng, H. Gu, R. Wan, In vitro comparison of the hemocompatibility of diamond-like carbon and carbon nitride coatings with different atomic percentages of N, Sci. China Life Sci. 55 (2012) 343–348, https://doi.org/10.1007/s11427-012-4308-9.

[29] H. Cao, J. Fu, Y. Liu, S. Chen, Facile design of superhydrophobic and superoleophilic copper mesh assisted by candle soot for oil water separation, Colloids Surf A Physicochem Eng Asp 537 (2018) 294–302, https://doi.org/10.1016/j.colsurfa.2017.09.055.

[30] G. Jena, R.P. George, J. Philip, Fabrication of a robust graphene oxide-nano SiO2-polydimethylsiloxane composite coating on carbon steel for marine applications, Prog. Org. Coat. 161 (2021) 106462, https://doi.org/10.1016/j.porgcoat.2021.106462.

[31] Y. Zeng, H. Cao, W. Jia, Y. Min, Q. Xu, An eco-friendly nitrogen doped carbon coating derived from chitosan macromolecule with enhanced corrosion inhibition on aluminum alloy, Surf. Coat. Technol. 445 (2022) 128709, https://doi.org/10.1016/j.surfcoat.2022.128709.

[32] M. Zhu, X. Li, Z. Zhang, P. Sun, X. Zang, K. Wang, M. Zhong, D. Wu, H. Zhu, Amorphous nitrogen doped carbon films: a novel corrosion resistant coating material, Adv. Eng. Mater. 16 (2014) 532–538, https://doi.org/10.1002/adem.201300408.

[33] D. Zander, N.A. Zumdick, Influence of Ca and Zn on the microstructure and corrosion of biodegradable Mg–Ca–Zn alloys, Corros. Sci. 93 (2015) 222–233, https://doi.org/10.1016/j.corsci.2015.01.027.

[34] Y. Sun, B. Zhang, Y. Wang, L. Geng, X. Jiao, Preparation and characterization of a new biomedical Mg–Zn–Ca alloy, Mater. Des. 34 (2012) 58–64, https://doi.org/10.1016/j.matdes.2011.07.058.

[35] H.R. Bakhsheshi-Rad, M.R. Abdul-Kadir, M.H. Idris, S. Farahany, Relationship between the corrosion behavior and the thermal characteristics and microstructure of Mg–0.5Ca–*x*Zn alloys, Corros. Sci. 64 (2012) 184–197, https://doi.org/10.1016/j.corsci.2012.07.015.

[36] J.C. Gao, S. Wu, Y. Wang, L.Y. Qiao, Study on corrosion and degradation behavior of Mg-Ca alloy in simulated body fluid, Mater. Sci. Forum 610–613 (2009) 942–945, https://doi.org/10.4028/www.scientific.net/MSF.610-613.942.

[37] S.R. Bare, F.D. Vila, M.E. Charochak, S. Prabhakar, W.J. Bradley, C. Jaye, D. A. Fischer, S.T. Hayashi, S.A. Bradley, J.J. Rehr, Characterization of coke on a Pt-Re/γ-Al2O3 Re-forming catalyst: experimental and theoretical study, ACS Catal. 7 (2017) 1452–1461, https://doi.org/10.1021/acscatal.6b02785.

[38] C.C. Zhang, S. Hartlaub, I. Petrovic, B. Yilmaz, Raman spectroscopy characterization of amorphous coke generated in industrial processes, ACS Omega 7 (2022) 2565–2570, https://doi.org/10.1021/acsomega.1c03456.

[39] S.I. Moseenkov, V.L. Kuznetsov, N.A. Zolotarev, B.A. Kolesov, I.P. Prosvirin, A. V. Ishchenko, A.V. Zavorin, Investigation of amorphous carbon in nanostructured carbon materials (a comparative study by TEM, XPS, Raman Spectroscopy and XRD), Materials 16 (2023) 1112, https://doi.org/10.3390/ma16031112.

[40] M. Noh, Y. Kwon, H. Lee, J. Cho, Y. Kim, M.G. Kim, Amorphous carbon-coated tin anode material for lithium secondary battery, Chem. Mater. 17 (2005) 1926–1929, https://doi.org/10.1021/cm0481372.

[41] J. Han, I. Johnson, Z. Lu, A. Kudo, M. Chen, Effect of local atomic structure on sodium ion storage in hard amorphous carbon, Nano Lett. 21 (2021) 6504–6510, https://doi.org/10.1021/acs.nanolett.1c01595.

[42] R. Ghasemi, A. Arab, S. Manouchehri, Tuning the dual-color fluorescence emission of nitrogen-doped carbon dots by changing nitrogen doping amounts, Russ J Gen Chem 93 (2023) 2161–2170, https://doi.org/10.1134/S1070363223080248.

[43] Q. Zhao, Z. Mou, B. Zhang, X. Zhang, Z. Wang, K. Wang, K. Gao, Q. Jia, Revealing the corrosion resistance of amorphous carbon films under heat shock via annealing, Diam. Relat. Mater. 102 (2020) 107692, https://doi.org/10.1016/j.diamond.2019.107692.

[44] G. Beamson, High Relution XPS of Organic Polymers. The Scienta ESCA 300 Database, ICIplc (1992), https://doi.org/10.1021/ed070pA25.5.

[45] A.V. Naumkin, A. Kraut-Vass, S.W. Gaarenstroom, Standard Reference Database, 20, Table of Content, 2012 . Version 4.1. 2012.
[46] M.C. Biesinger, Accessing the robustness of adventitious carbon for charge referencing (correction) purposes in XPS analysis: insights from a multi-user facility data review, Appl. Surf. Sci. 597 (2022) 153681, https://doi.org/10.1016/j.apsusc.2022.153681.
[47] A. Mohtasebi, T. Chowdhury, L.H.H. Hsu, M.C. Biesinger, P. Kruse, Interfacial charge transfer between phenyl-capped aniline tetramer films and iron oxide surfaces, J. Phys. Chem. C 120 (2016) 29248–29263, https://doi.org/10.1021/acs.jpcc.6b09950.
[48] J.F. Moulder, W.F. Stickle, P.E. Sobol, K.D. Bomben. Handbook of X-ray photoelectron spectroscopy. Chastain, J. Perkin-Elmer Corp., Eden Prairie, MN (1992).
[49] B.P. Singh, S. Nayak, K.K. Nanda, B.K. Jena, S. Bhattacharjee, L. Besra, The production of a corrosion resistant graphene reinforced composite coating on copper by electrophoretic deposition, Carbon 61 (2013) 47–56, https://doi.org/10.1016/j.carbon.2013.04.063.
[50] X. Gao, Y. Fu, D. Jiang, D. Wang, S. Xu, W. Liu, L. Weng, J. Yang, J. Sun, M. Hu, Constructing WS2/MoS2 nano-scale multilayer film and understanding its positive response to space environment, Surf. Coat. Technol. 353 (2018) 8–17, https://doi.org/10.1016/j.surfcoat.2018.08.072.
[51] D. Bootkul, B. Supsermpol, N. Saenphinit, C. Aramwit, S. Intarasiri, Nitrogen doping for adhesion improvement of DLC film deposited on Si substrate by Filtered Cathodic Vacuum Arc (FCVA) technique, Appl. Surf. Sci. 310 (2014) 284–292, https://doi.org/10.1016/j.apsusc.2014.03.059.
[52] N.W. Khun, E. Liu, X.T. Zeng, Corrosion behavior of nitrogen doped diamond-like carbon thin films in NaCl solutions, Corros. Sci. 51 (2009) 2158–2164, https://doi.org/10.1016/j.corsci.2009.05.050.
[53] C. Verma, A. Thakur, R. Ganjoo, S. Sharma, H. Assad, A. Kumar, M.A. Quraishi, A. Alfantazi, Coordination bonding and corrosion inhibition potential of nitrogen-rich heterocycles: azoles and triazines as specific examples, Coord. Chem. Rev. 488 (2023) 215177, https://doi.org/10.1016/j.ccr.2023.215177.
[54] A.V. Naumkin, A. Kraut-Vass, S.W. Gaarenstroom, C.J. Powell, NIST X-ray Photoelectron Spectroscopy Database Version 5.0, 2023, doi.org/10.18434/T4T88K.
[55] A. Abdal-hay, N.A.M. Barakat, J.K. Lim, Influence of electrospinning and dip-coating techniques on the degradation and cytocompatibility of Mg-based alloy, Colloids Surf A Physicochem Eng Asp 420 (2013) 37–45, https://doi.org/10.1016/j.colsurfa.2012.12.009.
[56] T.F. Conceicao, N. Scharnagl, C. Blawert, W. Dietzel, K.U. Kainer, Corrosion protection of magnesium alloy AZ31 sheets by spin coating process with poly(ether imide) [PEI], Corros. Sci. 52 (2010) 2066–2079, https://doi.org/10.1016/j.corsci.2010.02.027.
[57] R. Zhang, P.X. Ma, Biomimetic polymer/apatite composite scaffolds for mineralized tissue engineering, Macromol. Biosci. 4 (2004) 100–111, https://doi.org/10.1002/mabi.200300017.
[58] T.F. da Conceicao, N. Scharnagl, W. Dietzel, K.U. Kainer, On the degradation mechanism of corrosion protective poly(ether imide) coatings on magnesium AZ31 alloy, Corros. Sci. 52 (2010) 3155–3157, https://doi.org/10.1016/j.corsci.2010.06.008.
[59] U. Lelek-Borkowska, M. Wróbel, M. Marzec, P. Kustra, A. Milenin, Mg–Ca surgical wires degradation in animal serum, Metall Mater Trans A 55 (2024) 2141–2152, https://doi.org/10.1007/s11661-024-07387-8.
[60] A. Milenin, P. Kustra, U. Lelek-Borkowska, M. Wróbel, M. Marzec, J. Sulej-Chojnacka, J. Półrolniczak, I. Polkowska, B. Nowicka, In Vitro and In Vivo degradation of the new dissolvable surgical wire, Produced from Zn Based Low Alloy by Hot and Cold Drawing, Metall Mater Trans A 55 (2024) 3434–3449, https://doi.org/10.1007/s11661-024-07470-0.
[61] J. Zhang, S. Hou, M. Zhang, S. Zhang, W. Li, Corrosion resistance and biocompatibility of silica coatings on AZ31 magnesium alloy via magnetron sputtering, Mater. Today Commun. 41 (2024) 110890, https://doi.org/10.1016/j.mtcomm.2024.110890.
[62] G. Baril, G. Galicia, C. Deslouis, N. Pébère, B. Tribollet, V. Vivier, An impedance investigation of the mechanism of pure magnesium corrosion in sodium sulfate solutions, J. Electrochem. Soc. 154 (2006) C108, https://doi.org/10.1149/1.2401056.
[63] H. Krawiec, I. Kozina, M. Starowicz, M. Lekka, C. Zanella, L. Fedrizzi, M. Fedel, F. Deflorian, Corrosion rate and mechanism of degradation of Chitosan/TiO2 coatings deposited on MgZnCa alloy in Hank's solution, Int. J. Mol. Sci. 25 (2024) 5313, https://doi.org/10.3390/ijms25105313.
[64] D. Święch, K. Kollbek, P. Jabłoński, M. Gajewska, G. Palumbo, M. Oćwieja, N. Piergies, Exploring the nanoscale: AFM-IR visualization of cysteine adsorption on gold nanoparticles, Spectrochim. Acta A Mol. Biomol. Spectrosc. 318 (2024) 124433, https://doi.org/10.1016/j.saa.2024.124433.
[65] D. Święch, G. Palumbo, N. Piergies, K. Kollbek, M. Marzec, A. Szkudlarek, C. Paluszkiewicz, Surface modification of Cu nanoparticles coated commercial titanium in the presence of tryptophan: comprehensive electrochemical and spectroscopic investigations, Appl. Surf. Sci. 608 (2023) 155138, https://doi.org/10.1016/j.apsusc.2022.155138.
[66] D. Święch, N. Piergies, G. Palumbo, C. Paluszkiewicz, In situ and ex situ raman studies of cysteine's behavior on a titanium surface in buffer solution, Coatings 13 (2023) 175, https://doi.org/10.3390/coatings13010175.
[67] D. Święch, G. Palumbo, N. Piergies, E. Pięta, A. Szkudlarek, C. Paluszkiewicz, Spectroscopic investigations of 316L stainless steel under simulated inflammatory conditions for implant applications: the effect of tryptophan as corrosion inhibitor/hydrophobicity marker, Coatings 11 (2021) 1097, https://doi.org/10.3390/coatings11091097.
[68] E. Jablonská, J. Kubásek, D. Vojtěch, T. Ruml, J. Lipov, Test conditions can significantly affect the results of in vitro cytotoxicity testing of degradable metallic biomaterials, Sci Rep 11 (2021) 6628, https://doi.org/10.1038/s41598-021-85019-6.
[69] B. Zhang, Y. Hou, X. Wang, Y. Wang, L. Geng, Mechanical properties, degradation performance and cytotoxicity of Mg–Zn–Ca biomedical alloys with different compositions, Mater. Sci. Eng. C 31 (2011) 1667–1673, https://doi.org/10.1016/j.msec.2011.07.015.
[70] P. Yang, N. Huang, Y.X. Leng, Z.Q. Yao, H.F. Zhou, M. Maitz, Y. Leng, P.K. Chu, Wettability and biocompatibility of nitrogen-doped hydrogenated amorphous carbon films: effect of nitrogen, Nucl. Instrum. Methods Phys. Res., Sect. B 242 (2006) 22–25, https://doi.org/10.1016/j.nimb.2005.08.081.
[71] C. Pan, N. Yang, J. Chen, Q. Zhang, L. Deng, T. Luo, L. Meng, Bivalirudin functionalized hydrogel coating capable of catalytical NO-generation for enhanced anticorrosion and biocompatibility of magnesium alloy, Mater. Today Bio 31 (2025) 101473, https://doi.org/10.1016/j.mtbio.2025.101473.
[72] K. Jia, C. Zuo, Y. Xu, W. Ma, L. Wang, Y. Ji, J. Chen, Q. Zhang, C. Pan, T. Liu, Carboxymethyl chitosan/alendronate sodium/Sr2+ modified TiO2 nanotube arrays enhancing osteogenic activity and antibacterial property, Biomaterials Advances 167 (2025) 214107, https://doi.org/10.1016/j.bioadv.2024.214107.
[73] J. Chen, R. Xu, L. Meng, F. Yan, L. Wang, Y. Xu, Q. Zhang, W. Zhai, C. Pan, Biomimetic hydrogel coatings for improving the corrosion resistance, hemocompatibility, and endothelial cell growth of the magnesium alloy, Colloids Surf. B Biointerfaces 245 (2025) 114204, https://doi.org/10.1016/j.colsurfb.2024.114204.